



DNA damage reduces heterogeneity and coherence of chromatin motions

Maëlle Locatelli^{a,1}, Josh Lawrimore^{b,1}, Hua Lin^{c,1}, Sarvath Sanaulah^a, Clayton Seitz^c, Dave Segall^d, Paul Kefer^d, Naïke Salvador Moreno^a, Benton Lietz^a, Rebecca Anderson^a, Julia Holmes^a, Chongli Yuan^e, George Holzwarth^d, Kerry S. Bloom^b, Jing Liu^{c,f,g}, Keith Bonin^{d,h,2}, and Pierre-Alexandre Vidi^{a,h,i,2}

Edited by Karolin Luger, University of Colorado Boulder, Boulder, CO; received March 24, 2022; accepted June 7, 2022

Chromatin motions depend on and may regulate genome functions, in particular the DNA damage response. In yeast, DNA double-strand breaks (DSBs) globally increase chromatin diffusion, whereas in higher eukaryotes the impact of DSBs on chromatin dynamics is more nuanced. We mapped the motions of chromatin microdomains in mammalian cells using diffractive optics and photoactivatable chromatin probes and found a high level of spatial heterogeneity. DNA damage reduces heterogeneity and imposes spatially defined shifts in motions: Distal to DNA breaks, chromatin motions are globally reduced, whereas chromatin retains higher mobility at break sites. These effects are driven by context-dependent changes in chromatin compaction. Photoactivated lattices of chromatin microdomains are ideal to quantify microscale coupling of chromatin motion. We measured correlation distances up to 2 μm in the cell nucleus, spanning chromosome territories, and speculate that this correlation distance between chromatin microdomains corresponds to the physical separation of A and B compartments identified in chromosome conformation capture experiments. After DNA damage, chromatin motions become less correlated, a phenomenon driven by phase separation at DSBs. Our data indicate tight spatial control of chromatin motions after genomic insults, which may facilitate repair at the break sites and prevent deleterious contacts of DSBs, thereby reducing the risk of genomic rearrangements.

structured illumination | chromatin mobility | heterogeneity | DNA damage | phase separation

Chromatin is highly dynamic, and chromatin motions may influence most if not all genome functions including transcription, replication, and repair (1–5). Although the motions of individual chromatin loci are largely stochastic, these motions are primarily driven by adenosine triphosphate-dependent processes, not by heat alone (6–8). The high molecular weight and concentration of DNA macromolecules and their associated proteins have a dominant influence on chromatin motions. Chromatin movements are constrained by the polymeric nature of the DNA, physical obstacles within the nucleus, the viscosity of the nucleoplasm, and intra- and interfiber interactions, which lead to subdiffusive motions that can be described as an anomalous random walk (9, 10). In specific contexts, such as the DNA damage response (DDR), chromatin also exhibits directed motions, which are dependent on the actin and microtubule nucleoskeleton (11–13). Overall, phenotypical changes in the cell nucleus such as those caused by DNA damage alter chromatin dynamics. Reciprocally, chromatin motions may impact outcomes of the DDR.

Our current knowledge on chromatin motions is largely derived from yeast models, which have a strikingly different nuclear organization compared to higher eukaryotes (14). Most yeast studies show increased chromatin motions after DNA cleavage (15–18), which has been proposed to facilitate homology search during homologous recombination (HR) and may favor the assembly of “repair factories” (19). A study with mammalian cells found that DNA repair foci are more mobile than other nuclear regions (20). Moreover, dysfunctional telomeres (which mimic DNA double-strand breaks [DSBs]) move faster than capped and functional telomeres (21). Using a paired-particle tracking approach to measure the motions of chromatin microdomains at random nuclear locations, we previously found decreased diffusion in response to DNA damage (22). The discrepancy between these findings suggests that changes in chromatin dynamics in the DDR are time and context dependent.

Here, we used a structured illumination approach to map chromatin motions. Our results reveal spatial heterogeneity in chromatin dynamics in the cell nucleus. The results also reconcile contradictory observations by showing that DNA damage has differential effects on chromatin mobility depending on location. Mechanistically, these effects can be explained by changes in chromatin compaction. We also show that chromatin motions are coupled at the microscale and that DNA damage partially uncouples

Significance

Chromatin dynamics are profoundly altered during the DNA damage response, yet the spatial determinants and biophysical mechanisms underlying changes in chromatin kinetics remain poorly understood. We used structured illumination to visualize well-defined patterns of chromatin microdomains. We overlaid the resulting physical maps of chromatin dynamics with orthogonal readouts of DNA breaks and chromatin compaction in live cells. The approach, which simultaneously sampled chromatin in different nuclear regions, revealed the context dependency of the chromatin response to DNA damage. While we focus here on DNA damage, the approach has a broad spectrum of applications in genome biology.

Author contributions: M.L., G.H., K.S.B., J. Liu, K.B., and P.-A.V. designed research; M.L., S.S., N.S.M., B.L., R.A., J.H., and P.-A.V. performed research; P.K., C.V., G.H., and K.B. contributed new reagents/analytic tools; M.L., J. Lawrimore, H.L., S.S., C.S., D.S., J. Liu, K.B., and P.-A.V. analyzed data; and P.-A.V. wrote the paper.

The authors declare no competing interest.

This article is a PNAS Direct Submission.

Copyright © 2022 the Author(s). Published by PNAS. This article is distributed under Creative Commons Attribution-NonCommercial-NoDerivatives License 4.0 (CC BY-NC-ND).

¹M.L., J. Lawrimore, and H.L. contributed equally to this work.

²To whom correspondence may be addressed. Email: pierre.vidi@ico.unicancer.fr or bonin@wfu.edu.

This article contains supporting information online at <http://www.pnas.org/lookup/suppl/doi:10.1073/pnas.2205166119/-DCSupplemental>.

Published July 12, 2022.

chromatin motions. We present evidence that phase separation at DSBs is responsible for these alterations in chromatin motion correlation following genomic insults.

Results

Mapping chromatin microdomain motions reveals spatial heterogeneity of genome dynamics. To visualize chromatin motions in interphase nuclei, we applied structured illumination to U2OS osteosarcoma cells expressing low levels of histones H2A or H2B tagged with photoactivatable (PA) fluorescent proteins (PAGFP-H2A or PAmCherry-H2B; *SI Appendix, Fig. S1*). Arrays of photoactivated chromatin microdomains ($\sim 0.3 \mu\text{m}^2$) were generated using a diffractive optical element (23) (Fig. 1*A* and *B*), and spot motions within these arrays were tracked at subpixel resolution in time-lapse movies, enabling us to map chromatin diffusion simultaneously in different regions of the cell nucleus (Fig. 1*C*). Chemical fixation with paraformaldehyde almost entirely suppressed chromatin motions and strongly reduced motion heterogeneity, indicating a small contribution of noise to our measurements (Fig. 1*D*). Depletion of laminA/C was previously shown to increase diffusion of chromatin at telomeric regions (24) and significantly increased diffusion of photoactivated H2A microdomains (*SI Appendix, Fig. S2A*). We made the same observation in cells silencing the nuclear mitotic apparatus (NuMA) protein, a nucleoskeletal protein structurally related to lamins (*SI Appendix, Fig. S2B*). Conversely, overexpressing the proliferating cell nuclear antigen (PCNA), a DNA clamp, reduced chromatin motions in the S-phase (when PCNA binds sister chromatids), but not in G1/G2 phases [when the chromatin association of PCNA is less pronounced (25)] (*SI Appendix, Fig. S2C*).

Our approach revealed heterogeneity in chromatin motions between cells as well as within individual nuclei (Fig. 1*C*). This heterogeneity may reflect not only biological differences in chromatin dynamics imposed by nuclear architecture and chromatin state, but also measurement errors and the inherent stochasticity of mean squared displacement (MSD) analyses. To untangle these aspects, we measured chromatin microdomain motions twice in the same cells (Fig. 1*E*). We assumed that chromatin organization did not change substantially between the two back-to-back measurements (1 min apart) and that differences between the repeated measures largely reflected the stochasticity of chromatin dynamics as well as measurement errors. By extension, we considered reproducible heterogeneity (i.e., similarities between the paired measurements) as biologically relevant. As a first estimate of biological vs. methodological sources of heterogeneity, we identified all chromatin microdomains with diffusion values deviating by more than 50% from the cell median. We then determined whether the deviance was conserved in the second diffusion measurement of the same microdomain. We found that 25% of microdomains that were deviant in the first measurement deviated in the same way in the second measurement (i.e., with D values > 1.5 Med or < 0.5 Med). This was twice the rate expected by chance (13%; $P < 0.0001$; χ^2). In contrast, only 5% of spots deviated in opposite ways in the two measurements, which was significantly less than anticipated by chance (12%; $P < 0.0008$; χ^2). The remaining 75% of spots, deviant in only one of the two measurements, likely reflected technical sources of heterogeneity. Next, we calculated the Spearman correlation for the repeated measurements. Considering all paired measurements (from $n = 14$ cells), the correlation value was $r_s = 0.41$ ($P < 0.0001$). The r_s values calculated for each cell's repeated measures were

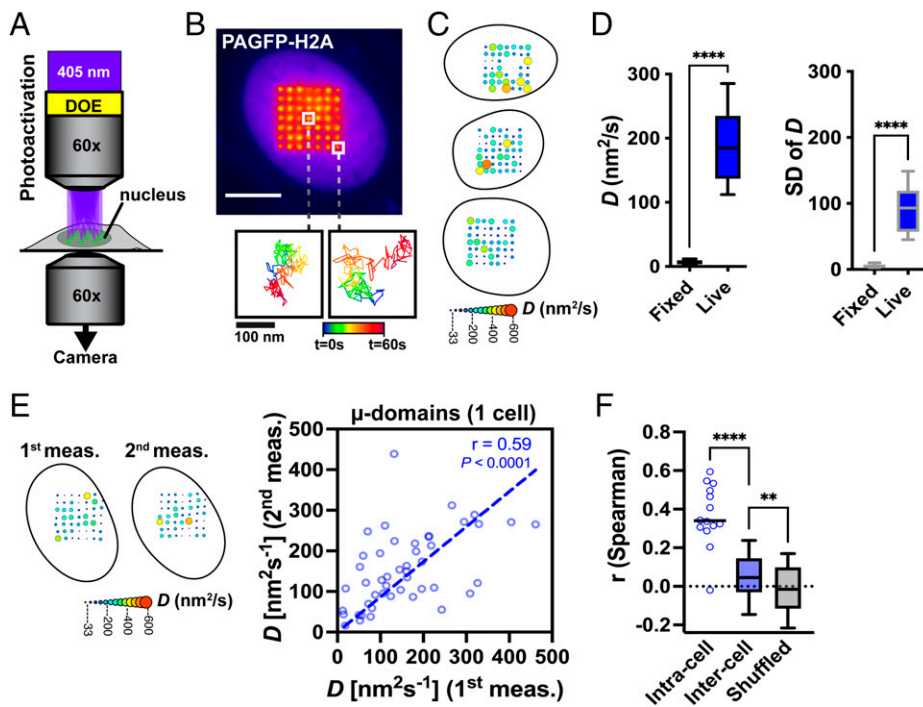


Fig. 1. Heterogeneity of chromatin motions. (A) Schematic of the structured illumination system used to project a grid of laser beamlets onto cell nuclei. DOE, diffractive optical element. (B) Array of photoactivated PAGFP-H2A spots in a U2OS cell nucleus. Traces of individual chromatin microdomains are shown for illustration (Scale bar, 10 μm). (C) Representative bubble plots used to visualize chromatin diffusion, D , in different regions of the cell nucleus. (D) Average chromatin diffusion and SD of D in fixed ($n = 28$) and live ($n = 52$) cells. **** $P < 0.0001$ (Mann-Whitney U test). (E) Repeated measures of D for individual microdomains in a cell. r , Spearman correlation coefficient. (F) Correlation (Spearman) of chromatin microdomain diffusion between repeated measurements of the same cell or between different cells. As a control, D values from the second measurements were shuffled, leading to an averaged $r = 0$, as expected. **** $P < 0.0001$; ** $P < 0.01$ (ANOVA and Tukey).

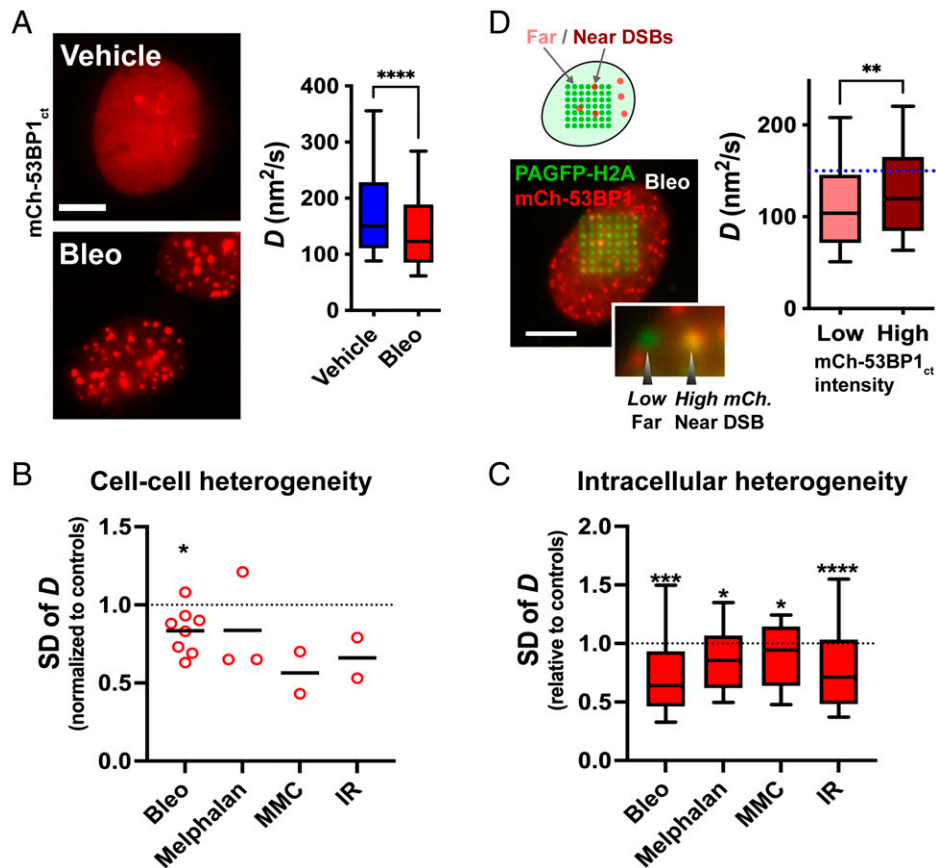


Fig. 2. Effect of DNA damage on the mobility of chromatin. (A) Chromatin microdomain diffusion in cells treated with bleomycin ($n = 403$) or vehicle ($n = 324$). $****P < 0.0001$ (Mann–Whitney U test). DNA damage is visualized with mCh-53BP1_{ct} foci. (B) SD of cell-averaged chromatin diffusion values (representing heterogeneity of the cell populations) in the different DNA damaging treatment conditions. The values are normalized to the controls (vehicle or nonirradiated cells). Each dot represents an individual dataset. $*P < 0.05$ (1-sample t test) (C) Averaged SD values of chromatin diffusion calculated for each cell (intracellular heterogeneity) and normalized to the corresponding controls. $*P < 0.05$; $***P < 0.0005$; $****P < 0.0001$ (1-sample t test). (D) Classification of chromatin microdomains (PAGFP-H2A) based on a DSB marker. Low intensity of mCh-53BP1_{ct} indicates a DSB-free region, whereas high mCh-53BP1_{ct} intensity indicates overlap with a DSB. Chromatin diffusion values in these two different regions are summarized in the graph. $**P < 0.01$ (Mann–Whitney U test; $n = 1,136$ and 141). The median value for vehicle-treated cells is indicated with a dashed line (Scale bars, $10 \mu\text{m}$).

significantly higher than the r_s values calculated between different cells (Fig. 1*F*). We conclude that biological heterogeneity contributes roughly half of the local differences in chromatin diffusion measured within a cell nucleus. Hence, tracking photoactivated chromatin microdomains captures heterogeneity in chromatin dynamics between cells and across cell nuclei, as well as altered chromatin motions after perturbing nucleoskeletal elements or chromatin tethers.

DNA damage reduces heterogeneity and induces spatially divergent shifts in chromatin dynamics. We induced DSBs with chemotherapeutics and ionizing radiation (IR) to analyze the effect of DNA damage on global chromatin mobility. DSBs were visualized with mCherry fused to the minimal DSB foci-forming region of p53-binding protein 1 (mCh-53BP1_{ct}; aa 1220–1711 [26, 27]). The expression of this DSB sensor, which colocalized with γ H2AX, did not alter chromatin microdomain motions (SI Appendix, Fig. S3*A* and *B*). The mCh-53BP1_{ct} sensor also showed that the 405 nm photoactivation laser did not cause DSBs in our experiments (SI Appendix, Fig. S4). The treatment of U2OS cells with the radiomimetic drug bleomycin led to a global reduction in chromatin diffusion (Fig. 2*A*), as reported previously (22). We made the same observation with the alkylating agent melphalan and 3 Gy IR. Similarly, the DNA cross-linker mitomycin C (MMC) reduced chromatin D , although the effect was modest and not significant (SI Appendix, Fig. S5*A*). The DNA damaging treatments also reduced

the heterogeneity of chromatin diffusion values between cells and within the nucleoplasm of a given cell (Fig. 2*B* and *C*).

To determine whether the effect of DNA damage on chromatin microdomain dynamics depends on the position of the microdomain relative to DNA break sites, we identified PAGFP-H2A spots overlapping with mCh-53BP1_{ct} and compared chromatin diffusion at and away from damage sites. As shown in Fig. 2*D*, chromatin diffusion at DSBs was significantly higher than in undamaged regions. These measurements reconcile our observations with the well-established acceleration of damage sites in yeasts (1). As an independent approach to assess global chromatin motions in response to DNA damage, DNA replication foci were labeled by the incorporation of fluorescent nucleotides (CF488-dUTP) (28) and tracked using confocal microscopy (SI Appendix, Fig. S5*B*). As expected, CF488-dUTP foci moved faster than PAGFP-H2A microdomains. Photoactivated PAGFP-H2A microdomains, which contain an estimated 40,000 histones, are indeed larger than the dUTP-labeled foci, and we previously showed experimentally and with computer simulations that the size of a chromatin array is inversely correlated with diffusion (29). Moreover, photoactivated histone microdomains capture collective motions from an ensemble of fibers. Individual fiber motions are likely averaged out. In contrast, dUTP foci are contiguous on chromatin molecules, leading to higher coupling (and therefore amplitudes) of motions. As observed with the photoactivation paradigm, DNA damage induction with bleomycin reduced the

heterogeneity of chromatin nanodomain diffusion by 16% (F test, $P < 0.0001$; compare box plots in *SI Appendix*, Fig. S5C). When considering regions of the nucleus distal from the DNA breaks, dUTP-labeled chromatin domains moved slower in bleomycin-treated cells compared to controls (*SI Appendix*, Fig. S5C). However, within nuclei with bleomycin damage, chromatin domains moved faster at repair sites than in undamaged regions (*SI Appendix*, Fig. S5D), confirming a divergent and spatially defined chromatin mobility response to genomic insults.

Repressive epigenetic marks enable a global reduction of chromatin motions after DNA damage. The drop in global chromatin microdomain motions after bleomycin treatment was measured during the entire interphase, although the effect was somewhat more pronounced in G1 and G2 (> 20% decrease of D) compared to the S phase (< 20% decrease of D) (*SI Appendix*, Fig. S6A–C). Interfering with DSB repair by nonhomologous end joining (NHEJ; KU80 silencing) and by HR (Rad51 silencing) did not prevent the drop in chromatin

motions after DNA damage, indicating that this global decrease in motions does not depend on functional DSB repair pathways (*SI Appendix*, Fig. S6D–F). DNA damage leads to the inhibition of transcription at the break sites (30–32) and globally (33, 34). However, RNA polymerase II inhibition with α -amanitin did not prevent the global decrease in chromatin microdomain motions following bleomycin treatment (*SI Appendix*, Fig. S6G), indicating that this effect is not mediated by the shutdown of transcription during the DNA damage response.

Chromatin domains labeled with fluorescent dUTPs had different sizes and intensities, reflecting distinct compaction levels (Fig. 3A). Overall, chromatin domain compaction and diffusion were anticorrelated in untreated cells (Spearman $r = -0.69$) as well as in bleomycin-treated cells ($r = -0.66$) (*SI Appendix*, Fig. S6H), suggesting that higher chromatin condensation leads to slower motions. Notably, in cells with DNA damage, chromatin compaction was higher in nuclear regions distal from DSBs compared to regions near damaged sites, mirroring differences in mobility (Fig. 3B).

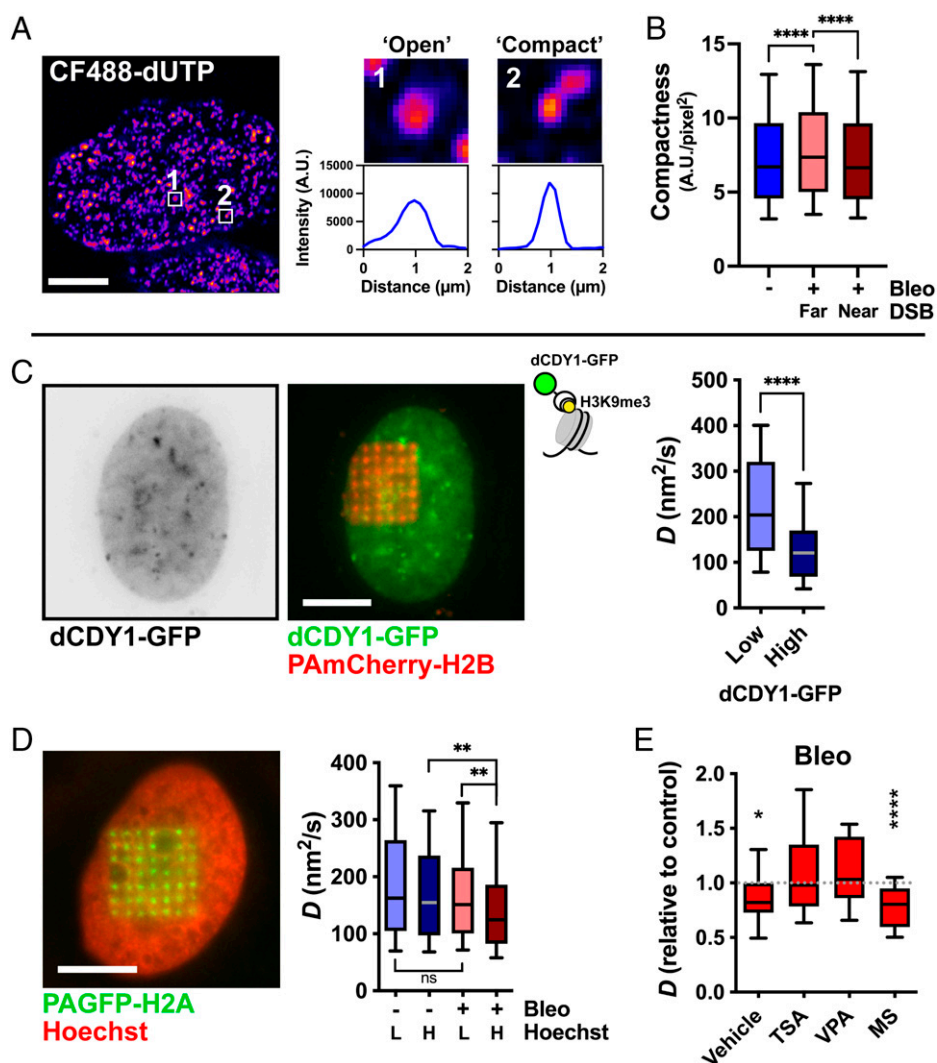


Fig. 3. Chromatin compaction distal from DSB sites causes a global decrease in chromatin microdomain motions. (A) Illustration of “open” and “compact” chromatin nanodomains in cells labeled with CF488-dUTPs, based on dUTP foci size and intensity. (B) Compactness of dUTP-labeled chromatin nanodomains in cells without DSB induction and in cells treated with bleomycin (Bleo). “Far” and “Near” refer to the position of the dUTP foci relative to DSBs defined by the mCh-53BP1ct foci (> 1 μm or \leq 1 μm , respectively). **** $P < 0.0001$ (Kruskal–Wallis and Dunn’s multiple comparison tests; $n > 50,000$ foci from 15 cells for each condition). A.U., arbitrary units. (C) Chromatin microdomain diffusion in nuclear regions with low or high H3K9me3, measured in PAmCherry-H2B cells expressing the dCDY1-GFP epigenetic sensor. **** $P < 0.0001$ (Mann–Whitney U test; $n = 45/52$). (D) Diffusion of chromatin microdomains in nuclear regions with low (L) or high (H) Hoechst intensity, in the absence or presence of bleomycin (Bleo). ** $P < 0.001$ (Kruskal–Wallis and Dunn’s multiple comparison tests; $n = 200$ –300). (E) Chromatin diffusion in bleomycin-treated cells (relative to controls) after cell exposures to TSA, VPA, and methylstat (MS). * $P < 0.05$; **** $P < 0.0001$ (Wilcoxon signed rank test; $n = 23$ –45) (Scale bars, 10 μm).

Treatment of U2OS cells with dimethyloxalylglycine (DMOG), which inhibits demethylation of histone H3 at lysine 9 (H3K9) (35), led to a marked accumulation of H3K9 trimethylation (H3K9me3) and reduced chromatin diffusion (*SI Appendix, Fig. S6*), indicating a connection between chromatin compaction and mobility. To further explore this connection, we expressed a fluorescent sensor to visualize H3K9me3 heterochromatin marks in live cells (dCDYI-GFP [36]). This sensor contains a fragment of the HP1 chromodomain fused to GFP. We confirmed overlap of the sensor with H3K9me3 detected by immunostaining (*SI Appendix, Fig. S3C*), then coexpressed dCDYI-GFP with PAmCherry-H2B and compared motions of fluorescent H2B microdomains in nuclear regions with high vs. low dCDYI-GFP intensity. In heterochromatin-rich regions (high dCDYI-GFP), the diffusion of chromatin microdomains was significantly slower than in euchromatin regions (with low dCDYI-GFP) (Fig. 3C). Next, we used Hoechst staining to estimate chromatin compaction. We validated that at the concentration used in our assays (0.1 $\mu\text{g}/\text{mL}$), Hoechst did not alter chromatin diffusion or the effect of DNA damage on chromatin diffusion (*SI Appendix, Fig. S6*). Note that cells stained with a higher concentration of Hoechst (10 $\mu\text{g}/\text{mL}$) had significantly slower chromatin microdomains than unstained cells. Strikingly, DSB induction with bleomycin reduced chromatin microdomain diffusion globally, but the effect was significantly

more pronounced in condensed regions with high Hoechst intensity (Fig. 3D). Accordingly, forcing an open chromatin state by treating cells with histone deacetylase inhibitors (trichostatin A [TSA] and valproic acid [VPA]) prevented the global chromatin motion reduction induced by bleomycin, whereas chromatin condensation with the demethylase inhibitor methylstat exacerbated the bleomycin-induced loss of motion (Fig. 3E). Collectively, these results show that chromatin condensation at nuclear regions distal from DSBs leads to a global reduction of chromatin dynamics.

Maps of chromatin diffusion reveal coherent motions of neighboring chromatin microdomains. With their known spot distances, the photoactivated lattices are ideal to assess whether chromatin microdomain motions are coupled at the microscale in the cell nucleus. We used the two-point correlation (TPC) function (37) to quantify motion correlations along the lines connecting the chromatin microdomain centers (Fig. 4A). The results showed a significant correlation between the nearest-neighbor (NN) microdomains, located 1.7 μm apart (Fig. 4B). As predicted (37), parallel TPC values were consistently higher than perpendicular TPC values (0.135 ± 0.038 vs. 0.031 ± 0.031 , respectively). Next-nearest neighbor spots (3N; 2.4 μm distance) were also significantly correlated, but the TPC values were lower than for NN. In contrast, next-next-nearest neighbors

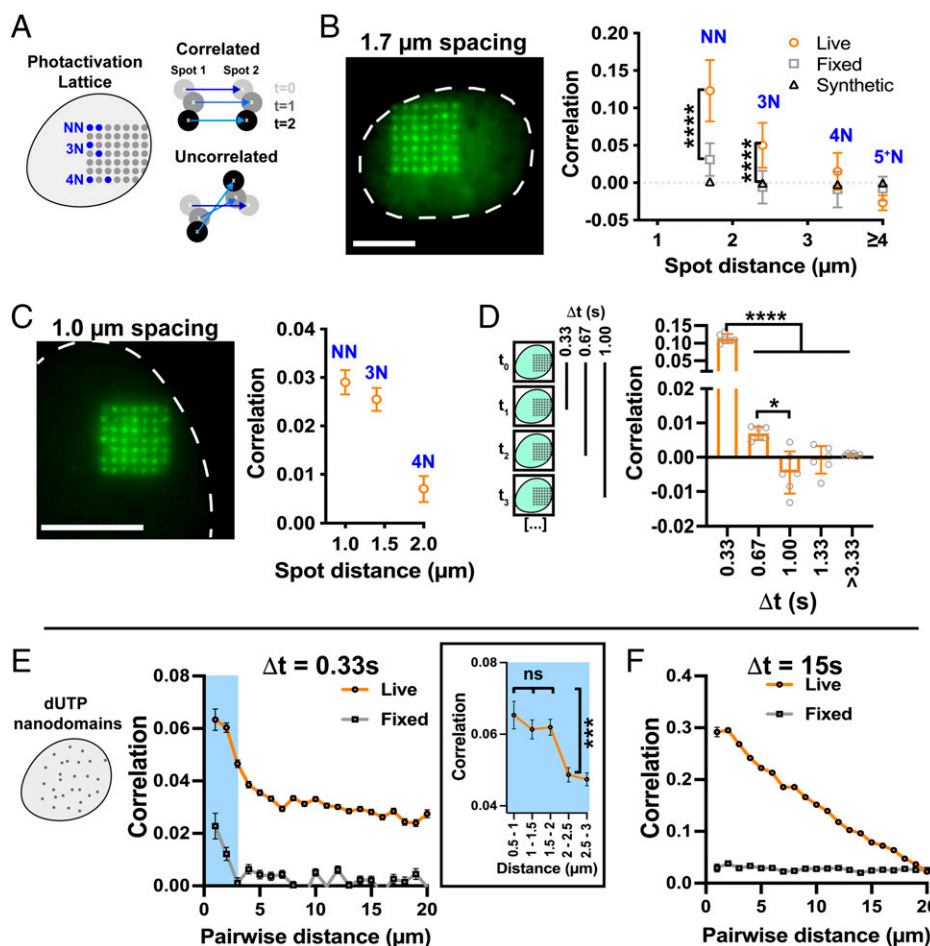


Fig. 4. Chromatin motions are correlated at the microscale. (A) Schematic illustrating pairs of spots with known distances in photoactivated grids of chromatin microdomains. NN (1.7 μm); 3N (2.4 μm); 4N (3.4 μm). (B) TPC of photoactivated PAGFP-H2A chromatin microdomains in live ($n = 73$) and fixed ($n = 28$) cells, as well as matching synthetic data ($n = 19$) with (uncorrelated) Brownian motions. The graph represents correlation values for the different classes of spot distances. **** $P < 0.0001$ (Kruskal-Wallis and Dunn's multiple comparison tests). 5⁺N, next-next-next nearest neighbors. (C) TPC of photoactivated PAGFP-H2A microdomains generated with a higher magnification objective, leading to tighter lattices. (D) Temporal dependence of chromatin microdomain correlation, calculated by skipping 1 ($\Delta t = 0.67$), 2 ($\Delta t = 1.00$), and further frames in the time-lapse movies. **** $P < 0.0001$; * $P < 0.05$ (ANOVA and Tukey's multiple comparison test). (E and F) TPC values for motions of chromatin domains labeled by fluorescent dUTPs in live and fixed cells, using either 0.33s (E) or 15s (F) time intervals. The inset in (E) shows correlation values for short nuclear distances, using smaller distance bins (Scale bars, 10 μm).

(4N; 3.4 μm) were very weakly correlated and spots separated by $\geq 4 \mu\text{m}$ were slightly anticorrelated. TPC values for NN and 3N microdomain pairs in live cells were significantly higher than those in fixed cells. The low TPC values in fixed cells indicate a small contribution of drift (corrected in our analyses) and system vibrations to correlation values in live cells. To further validate our approach, a synthetic dataset consisting of “cells” with lattices of spots with independent Brownian motions, and therefore no correlation, were analyzed and produced near-zero TPC values (Fig. 4B). Similar NN correlations and a decrease in correlations with increasing distances were measured for chromatin microdomains labeled with PAmCherry-H2B (SI Appendix, Fig. S7A).

Nuclei from a subset of cells ($\sim 10\%$) distorted noticeably in the time-lapse movies, and we assessed whether this phenomenon may have influenced microdomain correlation measures. Distortions were quantified by calculating cumulative changes in edge length (Δ_l) for the largest quadrilateral formed by the photoactivated lattice. The measures of distortion matched well with visual observations and were highly correlated with an independent angular metric of deformation (SI Appendix, Fig. S7B). As expected, distortions in fixed cells were lower than in live cells (SI Appendix, Fig. S7C). Notably, NN correlation values were independent of distortions, indicating that chromatin microdomain coherence did not merely reflect macroscale deformations of the cell nucleus (SI Appendix, Fig. S7D–E).

The mesh size of the photoactivation lattice is defined by the magnification of the photoactivation objective that focuses the laser beamlets onto the cell. To investigate chromatin correlations at lengths smaller than 1.7 μm , we used a photoactivation objective with a higher magnification (100 \times). With this alternative configuration, motions of NN spots (separated by 1.0 μm) and 3N spots (1.4 μm separation) had similar levels of correlation, whereas TPC values sharply dropped for 4N pairs (2.0 μm apart) (Fig. 4C). The correlations described above were obtained between one frame and the next ($\Delta t = 0.33 \text{ s}$). Next, we analyzed the time dependency of chromatin motion coupling by considering different time intervals in the movies. TPC values were calculated between frame N and N + 2 ($\Delta t = 0.67 \text{ s}$), between frame N and N + 3 ($\Delta t = 1 \text{ s}$), and so on. Correlations of NN motions sharply decreased at $\Delta t = 0.67 \text{ s}$ compared to $\Delta t = 0.33 \text{ s}$ (Fig. 4D).

As an independent approach to assess chromatin coherence, we quantified the correlation of motions for chromatin domains labeled with fluorescent dUTPs. This approach provided a continuous set of spot distances for TPC analyses. The results confirmed a coupled motion of chromatin at the microscale (Fig. 4E). Similar to our observations with photoactivated lattices, the correlation was highest for spots $\leq 2 \mu\text{m}$ apart and then decreased as a function of distance. Strikingly, both methods indicated correlated motions over a distance up to 1.5 to 2 μm . There were also interesting differences when comparing results derived from dUTP foci and photoactivated chromatin microdomains. In particular, dUTP foci correlations were higher at a larger time interval (15 s; Fig. 4F), unlike photoactivated microdomain correlations that were only measured at small time intervals. The different time dependencies for these correlated motions may depend on the scale considered or be due to technical differences between the two methods. Taken together, the results indicate chromatin coupling for physical distances of several micrometers in the cell nucleus.

Chromatin coherence spans across chromosome territories.

The physical range across which chromatin domain correlations are observed ($\sim 2 \mu\text{m}$) could be consistent with coherent motions of individual chromosomes. If this were the case, then

one would expect a bimodal distribution of TPC values, with higher correlations for spot pairs within a chromosome territory (CT) compared to pairs of spots in different CTs. However, our data indicated a unimodal distribution of TPC values (SI Appendix, Fig. S8A). To further assess whether motion coupling is limited to chromatin within individual CTs, we labeled CT boundaries using Cy5-dUTP (28). After two cycles of replication, the cells have (on average) half of their chromosomes labeled, and boundaries between CTs can be inferred. We validated this approach for labeling contiguous CT and detecting CT boundaries by using fluorescence in situ hybridization (FISH) painting of chromosome 1 (SI Appendix, Fig. S8B and C). Next, chromatin microdomains in photoactivated PAGFP-H2A lattices were annotated with the “variegated” Cy5-dUTP images (presence or absence of labeling). Spots in labeled and unlabeled regions had similar diffusion coefficients (SI Appendix, Fig. S8D), suggesting that the labeling method does not alter chromatin dynamics. When we performed guided TPC analysis with the CT annotations, we found only a small, nonsignificant decrease in NN correlation for chromatin microdomains across territories compared to spot pairs presumably located within a CT (SI Appendix, Fig. S8 E and F). The results suggest that correlated chromatin motions span chromosome territories.

DNA damage alters chromatin coherence. We compared TPC values for photoactivated chromatin microdomains after DNA damage induction with chemotherapeutics or ionizing radiation and found a significant decrease in correlated motions for bleomycin, melphalan, MMC, and IR treatments compared to controls (Fig. 5A and SI Appendix, Fig. S9A). Decreased correlations could not be explained by reduced global motions after DNA damage because treatments reducing chromatin diffusion do not necessarily alter coherence. For example, exposing cells to the G-quadruplex stabilizer BRACO-19 (a treatment that did not induce DSB in our experimental conditions) strongly reduced chromatin microdomain motions without significantly affecting TPC values (SI Appendix, Fig. S9B). Photobleaching was very similar in all treatment conditions, ruling out photobleaching dynamics as a potential source of artifacts (SI Appendix, Fig. S9C). We also compared the correlation of dUTP-labeled chromatin domains in cells with DNA damage and controls. In this case, bleomycin treatment increased nanodomain motion correlations (Fig. 5B) but led to a significant decrease in coherence length (Fig. 5C), suggesting that DNA damage constrains chromatin coherence at this physical scale. Next, we classified dUTP foci according to their proximity to mCh-53BP1_{ct} foci and found that chromatin domains near DSBs were significantly more correlated with one another than domains in undamaged regions (Fig. 5D).

Material properties of the nucleus alters chromatin coherence

in response to DNA damage. Several DNA repair factors, including 53BP1, undergo phase separation in the cell nucleus (38–43), yet the underlying roles and consequences of phase separation for genome maintenance are largely unknown. We reasoned that phase separation induced at DSBs during the DNA damage response might influence chromatin coherence at the microscale. To test this possibility, cells were pretreated with 1,6-hexanediol (1,6-HD), a chemical disrupting the weak molecular interactions necessary for liquid–liquid phase separation (LLPS). In line with previous observations (40, 41), 1,6-HD dissolved mCh-53BP1_{ct} condensates in cells with induced DSBs, and this effect was reversible (SI Appendix, Fig. S10A and B). As shown in Fig. 5E, the 1,6-HD treatment significantly inhibited

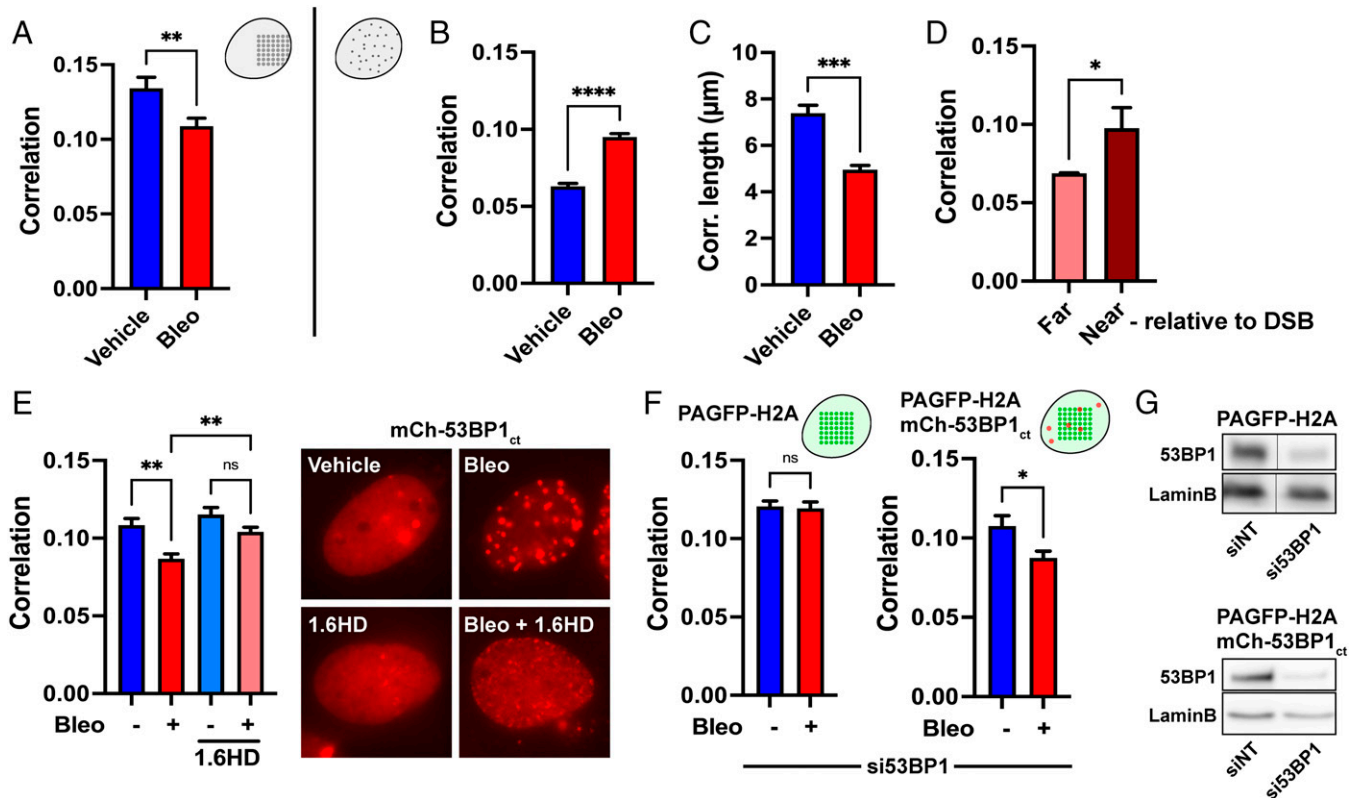


Fig. 5. Chromatin coherence decreases in response to DSBs. (A) Two-point correlation of photoactivated PAGFP-H2A chromatin microdomains (NN) in cells treated with bleomycin or vehicle. $**P < 0.005$ (Mann-Whitney U test; $n = 26$). (B-C) Correlation (B) and correlation length (C) for pairs of chromatin nanodomains labeled with fluorescent dUTPs. $****P < 0.0001$; $***P < 0.001$ (Mann-Whitney U test; $n = 8$ cells). (D) Chromatin nanodomain correlation, far ($n = 226,952$ foci) or near ($n = 78$ foci) DSBs labeled by mCh-53BP1ct. $*P < 0.05$ (Mann-Whitney U test). (E) Correlation of PAGFP-H2A chromatin microdomains in cells treated with 1,6-HD to disrupt LLPS, in the presence or absence of bleomycin. $**P < 0.005$; ns, not significant (Kruskal-Wallis and Dunn's multiple comparison tests; $n = 58-69$). (F) Chromatin microdomain correlation in PAGFP-H2A and PAGFP-H2A mCh-53BP1ct cells transfected with siRNA targeting 53BP1 (si53BP1) and treated with bleomycin as indicated. 53BP1 siRNA do not target the 53BP1ct fragment. $*P < 0.05$; ns, not significant (Mann-Whitney U test; $n = 32-38$). (G) Confirmation of 53BP1 silencing by Western blot in the two cell lines used in G. siNT, nontargeting siRNAs.

the loss of chromatin coherence following DSBs. Similarly, the inhibition of LLPS with ammonium acetate canceled the effect of DNA damage on chromatin microdomain coherence (SI Appendix, Fig. S10C). Since chemical treatments to interfere with phase separation may cause pleiotropic effects (44), we directly assessed the impact of 53BP1 condensates on chromatin microdomains by silencing the protein. The depletion of 53BP1 abrogated the drop in chromatin coherence in response to DSBs (Fig. 5F-G). The effect was rescued in cells expressing the C-terminal portion of 53BP1, which is sufficient for the formation of biomolecular condensates (40).

Discussion

We used well-defined lattices of photoactivated histones to track chromatin motions. This approach has the advantage of marking native chromatin, throughout the cell nucleus, and to yield generalizable results, which do not reflect specific chromosomal regions, artificial DNA arrays, or context-specific markers such as DSB repair foci. Particularly important for our study, this measurement method enables direct comparisons between cells with and without DNA damage. Tracking photoactivated chromatin microdomains revealed the spatial heterogeneity of chromatin dynamics, divergent responses to DNA damage, and microscale coupling of chromatin motions (Fig. 6). Previous studies have identified a high level of heterogeneity within individual cell nuclei and at multiple scales (24, 45-48). Sources of heterogeneity may be biological but also methodological: All experimental approaches

lead to location errors caused by motion blur (spot motions during acquisition) and imperfect fitting of particle positions. In addition, macromolecule diffusion in biological systems is an inherently stochastic process. This is true for chromatin, although mixed trajectories with both directed and random confined motions have been identified in the context of the DDR (2). Polymer models also yield heterogeneous diffusion values, even in the absence of monomer interactions (49-51), reflecting the randomness in MSD analyses. Repeating measures in the same cells revealed a cell-intrinsic component of heterogeneity in addition to stochasticity from random polymer motions and localization errors. Although correlation values for repeated measurements of the same cell were much higher than for measurements from independent cells (as expected), the latter were small but significantly higher than zero ($P = 0.0007$; 1-sample t test), suggesting some level of generalizable spatial heterogeneity (e.g., center vs. periphery of the nucleus).

The induction of DNA damage had two major effects on chromatin diffusion. First, the heterogeneity of chromatin dynamics decreased, both between cells and within cells. Second, the chromatin diffusion speed decreased globally yet remained higher at DSB sites. The second effect is not contradictory with the first. Indeed, the majority of our measurements were in DSB-free regions. Therefore, the few microdomains overlapping with DSBs had a minor impact on the SD (heterogeneity) of chromatin diffusion values. Most previous studies focused on chromatin motions at DSB sites and led to the consensus that DNA damage locally increases chromatin diffusion (15-17, 20, 46). Our

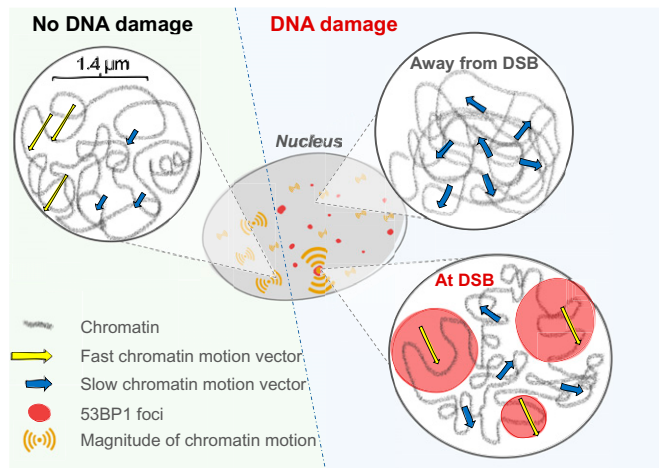


Fig. 6. Model for DNA damage-induced changes in chromatin dynamics. DNA damage reduces heterogeneity in chromatin dynamics, globally reduces chromatin motions (while chromatin displacements at break sites remain higher), and reduces the macroscale coherence of chromatin in the nucleus, which was measured over a range of 1.5 to 2 μm in our experiments.

finding that chromatin microdomains overlapping with DSB sites move faster than those in undamaged regions goes along with this consensus. The insight from our structured illumination approach is the spatial divergence in mammalian cells, with slower chromatin motions in the undamaged regions (Fig. 2). This contrasts with the situation in yeast, where DSBs increase chromatin diffusion throughout the nucleus (16, 18, 52). The nuclei of yeasts and higher eukaryotes differ in many ways. The size of the nucleus is much smaller in yeasts than in mammalian cells; the volume of an entire yeast nucleus approximates the size of a large DNA repair focus in a mammalian cell nucleus. With error-free HR predominating, yeast genomes may also be less prone to genomic rearrangements associated with chromatin motions (53) than mammalian genomes that mainly rely on NHEJ for DSB repair. Finally, *Saccharomyces cerevisiae* lacks key heterochromatin components found in mammalian cells such as HP1, which spreads heterochromatin by binding to and amplifying H3K9me₃.

Our results show that the global decrease in chromatin motions in response to DNA damage depends on chromatin compaction in undamaged regions (Fig. 3). The control of chromatin dynamics by compaction is not surprising: HP1 plays an important role in DSB repair (54, 55), and the transient formation of heterochromatin is an integral part of the DDR (56–59). Studies have shown global chromatin compaction distal from DNA breaks and local chromatin opening at DSB sites (60–62), reflecting our measurements with fluorescent dUTP foci. Moreover, slow nucleosome motions have been detected in peripheral, heterochromatin-rich regions (45), consistent with our findings. This concordance suggests that the effect of compaction on chromatin motions is conserved across scales (from nucleosomes to microdomains). A limitation of the results associating the compaction and diffusion of dUTP-labeled chromatin is that tracking precision may be higher for condensed vs. less condensed foci. This limitation, however, does not apply to our guided analyses of photoactivated grids that lead to the same conclusions. We predict that chromatin compaction and slower motions distal from DSBs reduce the frequency of chromosomal rearrangements. In hematopoietic stem/progenitor cells, lower H3K9me₃ levels have been measured at translocation hotspots (63). Moreover, increased telomere mobility has correlated with higher rates of telomeric fusions (21). This hypothesis deserves further investigation.

Our study identifies microscale coherence of chromatin motions, which is altered in the DDR. This finding is consistent with optical flow measurements (47, 48) and single-nucleosome analyses (64) and is supported here by two independent tracking paradigms, using either photoactivated histone microdomains or fluorescent dUTP foci, which correspond to distinct architectural scales (Fig. 4). The major difference between the two approaches was the time dependency of chromatin coherence. Within microdomains, correlated motions may average themselves out at larger timescales, which would explain the abrupt decrease in TPC with increasing time intervals. Remarkably, both approaches identified microscale coherence over a similar range, extending to 1.5 to 2 μm . A limitation of our approach is that we could not assess motion correlation at distances smaller than the spatial limit or the labeling methods (0.5–1 μm). Why chromatin motions are correlated over this particular distance remains to be established. The genome is divided into A and B compartments, corresponding to open and closed chromatin, with most chromatin–chromatin interactions occurring within a compartment (65). Simulations with polymer models suggest distinct dynamics of eu- and heterochromatin as well as correlated chromatin motions (49, 51, 66). These models also predict an average physical separation for chromatin in A vs. B compartments on the order of a micrometer (51), which is consistent with our experimental cutoff distance for coupled motions. We therefore propose that chromatin compartments may have distinct kinetics, insulated from one another.

DNA damage induction significantly reduced the microscale coherence of chromatin, and this effect could be blocked by perturbing phase separation (Fig. 4). LLPS is a major influencer of the higher-order organization of the genome (67–70). The formation of condensates may favor certain molecular interactions while preventing others by controlling the diffusion and concentration of factors in specific nuclear domains. Several DDR factors form large nuclear bodies reminiscent of LLPS at sites of DNA damage, the role of which is just emerging. DNA topoisomerase 2-binding protein 1 (TopBP1) condensates facilitate DDR signaling by the ataxia telangiectasia and Rad3-related (ATR) kinase (43), and the long noncoding RNA (lncRNA) LINP1 (lncRNA in non-homologous end joining pathway) promotes the multimerization of Ku heterodimers (KU70/KU80) and DSB synapsis via LLPS (71), whereas the phase separation of 53BP1 leads to the local enrichment of p53 (40). Nuclear condensates may also be mechanoactive. Artificial condensates were shown to restructure genome architecture, lowering chromatin density in specific regions by chromatin exclusion (72). Our finding that LLPS at DSB reduces chromatin microdomain coherence suggests a mechanism to kinetically insulate repair sites from the rest of the genome.

Materials and Methods

Cell lines, cell culture conditions, and transfection. U2OS osteosarcoma cells were cultured in DMEM supplemented with 10% fetal bovine serum (Gibco) at 37 °C, 5% CO₂ in a humidified incubator. Cultures were tested routinely for mycoplasma contamination; all tests were negative. For imaging, cells were seeded in 35 mm glass-bottom dishes (MatTek) at 100,000 cells per dish and cultured for 48 h. U2OS cells stably expressing PAGFP-H2A were generated by transfection of a PAGFP-H2A construct (obtained from J. Neefjes, Netherlands Cancer Institute) using lipofectamine 3000 (ThermoFisher) followed by clonal selection with geneticin. PAGFP-H2A was shown previously to associate with chromatin (22, 73). We confirmed the association of PAGFP-H2A with chromatin in the stable U2OS cell line by time-lapse imaging (SI Appendix, Fig. S1C). Similarly, a stable cell line expressing photoactivatable mCherry fused to H2B was generated by transfecting U2OS cells with a PAmCherry-H2B plasmid (obtained

from P. Cosma, Center for Genomic Regulation) followed by geneticin selection. To visualize DSBs, the U2OS PAGFP-H2A cell line was stably transfected with the mCherry-BP1-2 pLPC-Puro vector (obtained from T. de Lange, Rockefeller University, Addgene plasmid # 19835) with puromycin for clonal selection. In transient transfection experiments, cells were transfected using lipofectamine 3000 with plasmid DNA to express RFP-PCNA (obtained from C. Cardoso, Technische Universität Darmstadt) or with small interfering RNA (siRNA; Dharmacon, ON-TARGET plus SMARTpool; 50 nM). Cells were analyzed 72 h after siRNA transfection. For cell synchronization, the double thymidine block method was used as described in ref. (74).

Induction of DNA damage and other chemical treatments. DNA damage was induced by treating cells with bleomycin (20 mU/mL, 2 h), mitomycin C (MMC; 2.5 μ M, 18h), or melphalan (10 μ M, 24 h). Alternatively, cells were exposed to IR (3 Gy) using a portable X-ray tube, as described in ref. (75). TSA (100 nM, 4 h) and VPA (2 mM, 4 h) were used to inhibit histone deacetylation. Methylstat (2 μ M, 4 h) was used to inhibit histone trimethyl demethylases. DMOG (1 mM, 24 h) was used to modulate histone H3 methylation. To stabilize G-quadruplexes, cells were treated with BRACO-19 (100 mM, 5 d). To interfere with LLPS in the cell nucleus, cells were incubated with 1,6-HD (1.5%, 1 h) or with ammonium acetate (100 mM, 30 min). To inhibit RNA polymerase II, α -amanitin was applied to the cells (100 μ g/mL, 2 h). To fix cells, cultures were incubated in formalin solution (Sigma) for 20 min. Hoechst 33342 was used as a DNA stain.

Imaging of chromatin nanodomains. The scratch-replication labeling method was used to label chromatin domains of approximately 1 Mb (76). Briefly, a 20 μ L drop containing 50 μ M fluorescent dUTPs (CF488A-dUTP; Biotium) diluted in PBS was added to subconfluent U2OS cells. Cells were scraped with a sterile 26-gauge needle to induce transient cell membrane damage and incubated 1 min to allow entry of the fluorescent dUTPs. Culture medium was then added to the cells, which were imaged 24 h later. Image sequences were taken with a Zeiss LSM880 confocal microscope, using the AiryFast mode and a 40 \times water immersion objective (numerical aperture [NA] = 1.1). CF488A-dUTP and mCh-53BP1ct signals were simultaneously collected for 1 min with an imaging speed of 3.3 Hz. With these imaging conditions, there was no detectable photobleaching of dUTP-labeled chromatin foci. Cells were imaged in culture medium free of phenol red and were maintained at 37 $^{\circ}$ C, 5% CO₂ with a stage-top incubator and objective heater (PeCon). Chromatin domains labeled with dUTPs were identified and tracked as described in ref. (77).

Structured photoactivation and imaging of chromatin microdomains. The custom-built photoactivation module used to photoactivate chromatin microdomains in U2OS cells expressing photoactivatable histone reporters is described in ref. (23). Briefly, a diffractive optical element module is held by the condenser arm of an IX83 inverted microscope (Olympus) to generate a 7 \times 7 grid of near diffraction-limited beamlets of 405 nm light, focused on cell nuclei using a water-dipping objective (Nikon, 60 \times ; NA = 1.0). The irradiance at the sample is 170 mW/mm² (23), far below the phototoxic threshold measured in eukaryotic cells (78). The duration of the photoactivation pulse is 1 ms. Photoactivation beamlets generate PAGFP-H2A spots with a diameter (defined as the full width at half-maximum [FWHM] of the intensity profiles) of 600 \pm 70 nm. By comparison, FWHM values for mCh-53BP1ct foci were 700 \pm 200 nm (bleomycin-treated cells), 600 \pm 180 nm (melphalan), 550 \pm 130 nm (MMC), and 660 \pm 190 nm (IR). Images were taken with a 60 \times oil lens (NA = 1.35), the GFP cube set (470/40 EX; 525/5 EM), and a sCMOS camera (Hamamatsu ORCA-Flash 4.0), with an imaging speed of 3.3 Hz. Cells were kept at 37 $^{\circ}$ C in the custom enclosure of the microscope. The pH was maintained by using HEPES-based Live Cell Imaging Solution (Molecular Probes). Images were registered using the StackReg plugin in ImageJ (79). The tracking of chromatin microdomains was done in MATLAB, as described in ref. (23). To avoid the potential confounding effects of large nuclear deformation, cells with distortions greater than an arbitrary threshold ($\Delta L \geq 400$ pixels, with ΔL , the cumulative change in the perimeter of the largest quadrilateral defined by the grid of spots) were excluded from the analyses. To obtain tighter grids, the 60 \times objective used for photoactivation was replaced by a 100 \times water dipping objective (Nikon). To classify photoactivated microdomains based on the intensity of another fluorescent marker, we used custom MATLAB code to segment spots in the photoactivated grids and to

retrieve the boundary of the cell nucleus. Pixel intensities corresponding to the photoactivated spot regions were retrieved in the second fluorescent marker image and normalized to the average intensity of the marker calculated for the entire nuclear region.

Visualization of CTs. To label CTs, Cy5-dUTPs (50 μ M; Amersham) were loaded in cells, as described for chromatin nanodomain imaging. Cells were kept in culture for 50 h (2 doubling times) to allow segregation of labeled chromatids, leading to “variegated” chromosome labeling patterns, used to identify boundaries between chromosome territories. Cy5-dUTP images were pre-processed by applying Gaussian blur and gamma filtering before thresholding. The intensity corresponding to the position of all photoactivated PAGFP-H2A spots was retrieved. Pairs of NN spots were identified for which one spot had an intensity of zero (no Cy5-dUTP labeling) and the second spot an intensity of 255. These spot pairs were considered to be on different chromosomes. To validate this approach, chromosome 1 was detected using a whole-chromosome painting probe (CytoCell Aquarius) according to the FISH protocol of the provider in the variegated cells.

Analyses of chromatin domain correlations. We used the TPC function to quantify motion correlations along the lines connecting the centers of two points in the lattice, as described by Crocker and Hoffman (37). The TPC function is defined by

$$\rho^{\alpha\beta}(\tau) = \langle \Delta r_{\alpha}(t, \tau) \Delta r_{\beta}(t, \tau) \rangle. \quad [1]$$

The angle brackets indicate an average over all the observation times, t , and τ is the time interval between adjacent points in time. To compute the TPC function that yields the maximum correlation we use Eq. 1,

$$\Delta r_{\alpha}(t, \tau) = [\vec{r}_{\alpha}(t + \tau) - \vec{r}_{\alpha}(t)] \cdot \hat{r}_{loc}(t) \quad [2]$$

where \hat{r}_{loc} is the unit vector along the line-of-center direction between the two spots (α and β), and

$$\vec{r}_{\alpha}(t) = x_{\alpha}(t)\hat{x} + y_{\alpha}(t)\hat{y} \quad [3]$$

is the position vector of the spot labeled α at time t . We express the unit vector along the lines-of-center between spots α and β as

$$\hat{r}_{loc}(t) = \cos X(t)\hat{x} + \cos Y(t)\hat{y}, \quad [4]$$

where

$$\begin{aligned} \cos X &= \frac{x_{\beta}(t) - x_{\alpha}(t)}{r} \\ \cos Y &= \frac{y_{\beta}(t) - y_{\alpha}(t)}{r} \end{aligned} \quad [5]$$

$$r = \sqrt{(x_{\beta}(t) - x_{\alpha}(t))^2 + (y_{\beta}(t) - y_{\alpha}(t))^2}$$

Writing Eq. 1 out explicitly gives

$$\begin{aligned} \rho^{\alpha\beta}(\tau) &= \frac{\langle \Delta r_{\alpha}(t, \tau) \Delta r_{\beta}(t, \tau) \rangle}{\sqrt{\langle \Delta r_{\alpha}(t, \tau)^2 \rangle \langle \Delta r_{\beta}(t, \tau)^2 \rangle}} \\ &= \frac{\sum_{i=1}^N \Delta r_{\alpha}(t_i, \tau) \Delta r_{\beta}(t_i, \tau)}{\sqrt{\sum_{i=1}^N (\Delta r_{\alpha}(t_i, \tau)^2) \sum_{i=1}^N (\Delta r_{\beta}(t_i, \tau)^2)}} \end{aligned} \quad [6]$$

Analyses of cell distortions. To quantify nuclear distortions in movies from cells with photoactivated chromatin microdomains, two metrics based on the photoactivated grid pattern were considered: the cumulative change in the perimeter of the largest quadrilateral fitting the photoactivated grid of spots, ΔL (Eq. 7), and the cumulative angular changes of this quadrilateral, $\Delta\theta$ (Eq. 8),

$$\Delta L = \sum_{i=1}^{N-1} \sum_{k=1}^4 |L_k(i+1) - L_k(i)| \quad [7]$$

$$\Delta\theta = \sum_{i=1}^{N-1} \sum_{k=1}^4 |\theta_k(i+1) - \theta_k(i)|, \quad [8]$$

where N is the number of frames, the index k is a label for each of the 4 sides, L_k is the length of the k -th side of the i -th quadrilateral, and θ_k is the k -th angle of the i -th quadrilateral.

Immunofluorescence. Samples were rinsed with PBS, fixed 20 min with 10% formalin, washed with PBS glycine (50 mM), permeabilized 10 min with 0.5% Triton X-100, and blocked with 10% goat serum in immunofluorescence (IF) buffer (130 mM NaCl, 13.2 mM Na₂HPO₄, 3.5 mM NaH₂PO₄, 0.1% bovine serum albumin, 0.05% NaN₃, 0.2% Triton X-100, and 0.05% Tween 20). Samples were incubated overnight at 4 °C with primary antibodies diluted in blocking buffer. After three washes with IF buffer, samples were incubated with secondary antibodies (4 µg/mL) and washed again with IF. Primary antibodies were against γH2AX (Millipore, clone JBW301; 2 µg/mL), H3K9me3 (Cell Signaling, clone D4W1U; 1:800), KU80 (Abcam, catalog number ab119935; 2 µg/mL), laminA/C (Santa Cruz, catalog number SC-7292; 4 µg/mL), NuMA (clone B1C11, a gift from J. Nickerson, University of Massachusetts; 1:2 dilution), and Rad51 (AbCam, catalog number Ab63801; 1:300). Secondary antibodies were anti-mouse AlexaFluor-488 and anti-rabbit AlexaFluor-568 (both from Life Technologies; 1:500). Cell labeling with 5-ethynyl-2'-deoxyuridine was done using Click-iT reagents (Invitrogen). Nuclei were stained with 0.5 µg/mL DAPI. Samples were mounted using ProLong Gold antifade (Molecular Probes) and imaged with an IX83 Olympus microscope, using a 60× oil immersion objective (NA = 1.35) and the appropriate filter cubes (Chroma).

Immunoblotting. Cells were lysed with 2% SDS in PBS. Protein concentrations were determined with the DC protein assay (BioRad). Equal amounts of proteins were resolved by SDS-PAGE and transferred onto nitrocellulose membranes for immunoblotting with antibodies against 53BP1 (AbCam, catalog number Ab36823; 1 µg/mL), histone H2A (Cell Signaling, clone D603A; 1:1,000), histone H2B (AbCam, catalog number Ab1790; 1:1,000), histone H3 (AbCam, clone 1B1B2; 1:500), H3K9me3 (Cell Signaling, clone D4W1U; 1:800), KU80 (Abcam, catalog number ab119935; 1 µg/mL), laminB (AbCam, catalog number Ab16048; 0.2 µg/mL), and Rad51 (AbCam, catalog number Ab63801; 1:1,000).

Enhanced chemiluminescence signals were detected with an Amersham Imager 600.

Statistical analyses. Statistical analyses were done using GraphPad Prism 9. The D'Agostino & Pearson omnibus normality test was used to test for normality. Nonparametric tests were used if the data did not pass the normality test (at alpha = 0.05). Statistical tests are indicated in the figure legends. *P* values ≤ 0.05 were considered significant. All statistical tests were 2-sided. Unless specified otherwise, *N* corresponds to the number of cells analyzed in each condition.

Data Availability. All study data are included in the article and/or *SI Appendix*.

ACKNOWLEDGMENTS. We thank Dr. Jacques Neeffes (Netherlands Cancer Institute) for providing the PAGFP-H2A DNA construct and Dr. T. de Lange (Rockefeller University) for providing the mCherry-53BP1ct DNA construct. This work was funded by the National Cancer Institute (U01CA214282 and P30CA012197 to the Wake Forest Baptist Comprehensive Cancer Center) and the Wake Forest Center for Molecular Signaling via its imaging facility.

- C. J. Lawrimore, J. Lawrimore, Y. He, S. Chavez, K. Bloom, Polymer perspective of genome mobilization. *Mutat. Res.* **821**, 111706 (2020).
- J. Miné-Hattab, I. Chiolo, Complex chromatin motions for DNA repair. *Front. Genet.* **11**, 800 (2020).
- A. Seeber, M. H. Hauer, S. M. Gasser, Chromosome dynamics in response to DNA damage. *Annu. Rev. Genet.* **52**, 295–319 (2018).
- M. Babokhov, K. Hibino, Y. Itoh, K. Maeshima, Local chromatin motion and transcription. *J. Mol. Biol.* **432**, 694–700 (2020).
- C. Zimmer, E. Fabre, Chromatin mobility upon DNA damage: State of the art and remaining questions. *Curr. Genet.* **65**, 1–9 (2019).
- W. F. Marshall *et al.*, Interphase chromosomes undergo constrained diffusional motion in living cells. *Curr. Biol.* **7**, 930–939 (1997).
- K. Wiesmeijer, I. M. Krouwels, H. J. Tanke, R. W. Dirks, Chromatin movement visualized with photoactivable GFP-labeled histone H4. *Differentiation* **76**, 83–90 (2008).
- S. C. Weber, A. J. Spakowitz, J. A. Theriot, Nonthermal ATP-dependent fluctuations contribute to the in vivo motion of chromosomal loci. *Proc. Natl. Acad. Sci. U.S.A.* **109**, 7338–7343 (2012).
- H. Hajjoui *et al.*, High-throughput chromatin motion tracking in living yeast reveals the flexibility of the fiber throughout the genome. *Genome Res.* **23**, 1829–1838 (2013).
- J. Miné-Hattab, V. Recamier, I. Izeldin, R. Rothstein, X. Darzacq, Multi-scale tracking reveals scale-dependent chromatin dynamics after DNA damage. *Mol. Biol. Cell* **28**, 3323–3332 (2017).
- C. P. Caridi *et al.*, Nuclear F-actin and myosins drive relocalization of heterochromatic breaks. *Nature* **559**, 54–60 (2018).
- B. R. Schrank *et al.*, Nuclear ARP2/3 drives DNA break clustering for homology-directed repair. *Nature* **559**, 61–66 (2018).
- R. Oshidari *et al.*, Nuclear microtubule filaments mediate non-linear directional motion of chromatin and promote DNA repair. *Nat. Commun.* **9**, 2567 (2018).
- T. Misteli, E. Soutoglou, The emerging role of nuclear architecture in DNA repair and genome maintenance. *Nat. Rev. Mol. Cell Biol.* **10**, 243–254 (2009).
- V. Dion, V. Kalck, C. Horigome, B. D. Towbin, S. M. Gasser, Increased mobility of double-strand breaks requires Mec1, Rad9 and the homologous recombination machinery. *Nat. Cell Biol.* **14**, 502–509 (2012).
- J. Miné-Hattab, R. Rothstein, Increased chromosome mobility facilitates homology search during recombination. *Nat. Cell Biol.* **14**, 510–517 (2012).
- S. Herbert *et al.*, Chromatin stiffening underlies enhanced locus mobility after DNA damage in budding yeast. *EMBO J.* **36**, 2595–2608 (2017).
- J. Lawrimore *et al.*, Microtubule dynamics drive enhanced chromatin motion and mobilize telomeres in response to DNA damage. *Mol. Biol. Cell* **28**, 1701–1711 (2017).
- V. Dion, S. M. Gasser, Chromatin movement in the maintenance of genome stability. *Cell* **152**, 1355–1364 (2013).
- P. M. Krawczyk *et al.*, Chromatin mobility is increased at sites of DNA double-strand breaks. *J. Cell Sci.* **125**, 2127–2133 (2012).
- N. Dimitrova, Y. C. Chen, D. L. Spector, T. de Lange, 53BP1 promotes non-homologous end joining of telomeres by increasing chromatin mobility. *Nature* **456**, 524–528 (2008).
- J. Liu, P. A. Vidi, S. A. Lelièvre, J. M. Irudayaraj, Nanoscale histone localization in live cells reveals reduced chromatin mobility in response to DNA damage. *J. Cell Sci.* **128**, 599–604 (2015).
- K. Bonin *et al.*, Structured illumination to spatially map chromatin motions. *J. Biomed. Opt.* **23**, 1–8 (2018).
- I. Bronshtein *et al.*, Loss of lamin A function increases chromatin dynamics in the nuclear interior. *Nat. Commun.* **6**, 8044 (2015).
- J. Essers *et al.*, Nuclear dynamics of PCNA in DNA replication and repair. *Mol. Cell. Biol.* **25**, 9350–9359 (2005).
- O. Zgheib, K. Pataky, J. Brugger, T. D. Halazonetis, An oligomerized 53BP1 tudor domain suffices for recognition of DNA double-strand breaks. *Mol. Cell. Biol.* **29**, 1050–1058 (2009).
- C. Escibano-Díaz *et al.*, A cell cycle-dependent regulatory circuit composed of 53BP1-RIF1 and BRCA1-CtIP controls DNA repair pathway choice. *Mol. Cell* **49**, 872–883 (2013).
- E. M. Manders, H. Kimura, P. R. Cook, Direct imaging of DNA in living cells reveals the dynamics of chromosome formation. *J. Cell Biol.* **144**, 813–821 (1999).
- J. Lawrimore *et al.*, ChromoShake: A chromosome dynamics simulator reveals that chromatin loops stiffen centromeric chromatin. *Mol. Biol. Cell* **27**, 153–166 (2016).
- N. M. Shanbhag, I. U. Rafalska-Metcalf, C. Balane-Bolivar, S. M. Janicki, R. A. Greenberg, ATM-dependent chromatin changes silence transcription in cis to DNA double-strand breaks. *Cell* **141**, 970–981 (2010).
- C. Meisenberg *et al.*, Repression of transcription at DNA breaks requires cohesin throughout interphase and prevents genome instability. *Mol. Cell* **73**, 212–223.e7 (2019).
- A. C. Vitor *et al.*, Single-molecule imaging of transcription at damaged chromatin. *Sci. Adv.* **5**, eaau1249 (2019).
- M. Kruhlik *et al.*, The ATM repair pathway inhibits RNA polymerase I transcription in response to chromosome breaks. *Nature* **447**, 730–734 (2007).
- G. F. Heine, A. A. Horwitz, J. D. Parvin, Multiple mechanisms contribute to inhibit transcription in response to DNA damage. *J. Biol. Chem.* **283**, 9555–9561 (2008).
- M. K. Ayrapetov *et al.*, Activation of Hif1α by the polyhydroxylase inhibitor dimethylxylglycine decreases radiosensitivity. *PLoS One* **6**, e26064 (2011).
- O. F. Sánchez, A. Mendonca, A. Min, J. Liu, C. Yuan, Monitoring histone methylation (H3K9me3) changes in live cells. *ACS Omega* **4**, 13250–13259 (2019).
- J. C. Crocker, B. D. Hoffman, Multiple-particle tracking and two-point microrheology in cells. *Methods Cell Biol.* **83**, 141–178 (2007).
- M. Altmeyer *et al.*, Liquid demixing of intrinsically disordered proteins is seeded by poly(ADP-ribose). *Nat. Commun.* **6**, 8088 (2015).
- A. Patel *et al.*, A liquid-to-solid phase transition of the ALS protein FUS accelerated by disease mutation. *Cell* **162**, 1066–1077 (2015).
- S. Kilic *et al.*, Phase separation of 53BP1 determines liquid-like behavior of DNA repair compartments. *EMBO J.* **38**, e101379 (2019).
- F. Pessina *et al.*, Functional transcription promoters at DNA double-strand breaks mediate RNA-driven phase separation of damage-response factors. *Nat. Cell Biol.* **21**, 1286–1299 (2019).
- R. Oshidari *et al.*, DNA repair by Rad52 liquid droplets. *Nat. Commun.* **11**, 695 (2020).
- C. Frattini *et al.*, TopBP1 assembles nuclear condensates to switch on ATR signaling. *Mol. Cell* **81**, 1231–1245.e8 (2021).
- R. Düster, I. H. Kaltheuner, M. Schmitz, M. Geyer, 1,6-hexanediol, commonly used to dissolve liquid-liquid phase separated condensates, directly impairs kinase and phosphatase activities. *J. Biol. Chem.* **296**, 100260 (2021).
- S. S. Ashwin, T. Nozaki, K. Maeshima, M. Sasaki, Organization of fast and slow chromatin revealed by single-nucleosome dynamics. *Proc. Natl. Acad. Sci. U.S.A.* **116**, 19939–19944 (2019).
- F. Lotterberger, R. A. Karssemeijer, N. Dimitrova, T. de Lange, 53BP1 and the LINC complex promote microtubule-dependent DSB mobility and DNA repair. *Cell* **163**, 880–893 (2015).
- A. Zidovska, D. A. Weitz, T. J. Mitchison, Micron-scale coherence in interphase chromatin dynamics. *Proc. Natl. Acad. Sci. U.S.A.* **110**, 15555–15560 (2013).
- H. A. Shaban, R. Barth, L. Recoules, K. Bystrycky, Hi-D: Nanoscale mapping of nuclear dynamics in single living cells. *Genome Biol.* **21**, 95 (2020).

49. G. Shi, L. Liu, C. Hyeon, D. Thirumalai, Interphase human chromosome exhibits out of equilibrium glassy dynamics. *Nat. Commun.* **9**, 3161 (2018).
50. Y. He *et al.*, Statistical mechanics of chromosomes: In vivo and in silico approaches reveal high-level organization and structure arise exclusively through mechanical feedback between loop extruders and chromatin substrate properties. *Nucleic Acids Res.* **48**, 11284–11303 (2020).
51. H. Salari, M. Di Stefano, D. Jost, Spatial organization of chromosomes leads to heterogeneous chromatin motion and drives the liquid- or gel-like dynamical behavior of chromatin. *Genome Res.* **32**, 28–43 (2022).
52. M. H. Hauer *et al.*, Histone degradation in response to DNA damage enhances chromatin dynamics and recombination rates. *Nat. Struct. Mol. Biol.* **24**, 99–107 (2017).
53. V. Roukos, B. Burman, T. Misteli, The cellular etiology of chromosome translocations. *Curr. Opin. Cell Biol.* **25**, 357–364 (2013).
54. N. Ayoub, A. D. Jeyasekharan, J. A. Bernal, A. R. Venkitaraman, HP1-beta mobilization promotes chromatin changes that initiate the DNA damage response. *Nature* **453**, 682–686 (2008).
55. M. S. Luijsterburg *et al.*, Heterochromatin protein 1 is recruited to various types of DNA damage. *J. Cell Biol.* **185**, 577–586 (2009).
56. M. K. Ayrapetov, O. Gursoy-Yuzugullu, C. Xu, Y. Xu, B. D. Price, DNA double-strand breaks promote methylation of histone H3 on lysine 9 and transient formation of repressive chromatin. *Proc. Natl. Acad. Sci. U.S.A.* **111**, 9169–9174 (2014).
57. R. C. Burgess, B. Burman, M. J. Kruhlik, T. Misteli, Activation of DNA damage response signaling by condensed chromatin. *Cell Rep.* **9**, 1703–1717 (2014).
58. S. Khurana *et al.*, A macrohistone variant links dynamic chromatin compaction to BRCA1-dependent genome maintenance. *Cell Rep.* **8**, 1049–1062 (2014).
59. L. Li *et al.*, SIRT7 is a histone desuccinylase that functionally links to chromatin compaction and genome stability. *Nat. Commun.* **7**, 12235 (2016).
60. E. Hinde, X. Kong, K. Yokomori, E. Gratton, Chromatin dynamics during DNA repair revealed by pair correlation analysis of molecular flow in the nucleus. *Biophys. J.* **107**, 55–65 (2014).
61. J. Lou *et al.*, Phasor histone FLIM-FRET microscopy quantifies spatiotemporal rearrangement of chromatin architecture during the DNA damage response. *Proc. Natl. Acad. Sci. U.S.A.* **116**, 7323–7332 (2019).
62. J. Lou, A. Solano, Z. Liang, E. Hinde, Phasor histone FLIM-FRET microscopy maps nuclear-wide nanoscale chromatin architecture with respect to genetically induced DNA double-strand breaks. *Front. Genet.* **12**, 770081 (2021).
63. B. Burman, Z. Z. Zhang, G. Pegoraro, J. D. Lieb, T. Misteli, Histone modifications predispose genome regions to breakage and translocation. *Genes Dev.* **29**, 1393–1402 (2015).
64. T. Nozaki *et al.*, Dynamic organization of chromatin domains revealed by super-resolution live-cell imaging. *Mol. Cell* **67**, 282–293.e7 (2017).
65. E. Lieberman-Aiden *et al.*, Comprehensive mapping of long-range interactions reveals folding principles of the human genome. *Science* **326**, 289–293 (2009).
66. M. Di Pierro, B. Zhang, E. L. Aiden, P. G. Wolynes, J. N. Onuchic, Transferable model for chromosome architecture. *Proc. Natl. Acad. Sci. U.S.A.* **113**, 12168–12173 (2016).
67. C. Hult *et al.*, Enrichment of dynamic chromosomal crosslinks drive phase separation of the nucleolus. *Nucleic Acids Res.* **45**, 11159–11173 (2017).
68. A. R. Strom *et al.*, Phase separation drives heterochromatin domain formation. *Nature* **547**, 241–245 (2017).
69. A. G. Larson *et al.*, Liquid droplet formation by HP1 α suggests a role for phase separation in heterochromatin. *Nature* **547**, 236–240 (2017).
70. B. A. Gibson *et al.*, Organization of chromatin by intrinsic and regulated phase separation. *Cell* **179**, 470–484.e21 (2019).
71. R. Thapar *et al.*, Mechanism of efficient double-strand break repair by a long non-coding RNA. *Nucleic Acids Res.* **48**, 10953–10972 (2020).
72. Y. Shin *et al.*, Liquid nuclear condensates mechanically sense and restructure the genome. *Cell* **175**, 1481–1491.e13 (2018).
73. B. Pang *et al.*, Drug-induced histone eviction from open chromatin contributes to the chemotherapeutic effects of doxorubicin. *Nat. Commun.* **4**, 1908 (2013).
74. J. V. Harper, Synchronization of cell populations in G1/S and G2/M phases of the cell cycle. *Methods Mol. Biol.* **296**, 157–166 (2005).
75. S. Prajapati *et al.*, Characterization and implementation of a miniature X-ray system for live cell microscopy. *Mutat. Res.* **824**, 111772 (2022).
76. J. Walter, L. Schermelleh, M. Cremer, S. Tashiro, T. Cremer, Chromosome order in HeLa cells changes during mitosis and early G1, but is stably maintained during subsequent interphase stages. *J. Cell Biol.* **160**, 685–697 (2003).
77. P. Kefer *et al.*, Performance of deep learning restoration methods for the extraction of particle dynamics in noisy microscopy image sequences. *Mol. Biol. Cell* **32**, 903–914 (2021).
78. P. M. Carlton *et al.*, Fast live simultaneous multiwavelength four-dimensional optical microscopy. *Proc. Natl. Acad. Sci. U.S.A.* **107**, 16016–16022 (2010).
79. P. Thévenaz, U. E. Ruttimann, M. Unser, A pyramid approach to subpixel registration based on intensity. *IEEE Trans. Image Process.* **7**, 27–41 (1998).